

INTRODUCTION

Above Earth's atmosphere are the Van Allen radiation belts, a complex and dynamic plasma environment that can effect our technology-driven society. These effects include: a higher radiation dose for astronauts and cosmonauts, higher chance of spacecraft failure due to single event upsets that can lead to catastrophic latchups, cumulative degradation of silicon (changing the silicon doping) from an extended radiation dose that can degrade a transition to the point where it no longer functions as a switch, and the degradation of the ozone layer due to the chemical production of NOX and HOX. With these effects in mind, it is no surprise that the radiation belts have been extensively studied since their discovery in the 1960s.

A topic of interest in the space physics community is wave-particle intersections that as we will see later in the introduction, can accelerate particles and scatter them into the atmosphere.

The goal of this dissertation is to study the wave-particle mechanism that scatters microbursts into Earth's atmosphere. This goal will be achieved by first introducing single charged particle motion in electric and magnetic fields, the major particle populations and how they couple in the magnetosphere, and then describe the history and current state of the fields relating to microbursts and wave-particle scattering

Charged Particle Motion in Electric and Magnetic Fields

A charged particle trapped in the magnetosphere will experience three types of periodic motion in Earth's nearly dipolar field. The three motions are ultimately due to the Lorentz force that a particle of momentum \vec{p} , charge q , and velocity \vec{v}

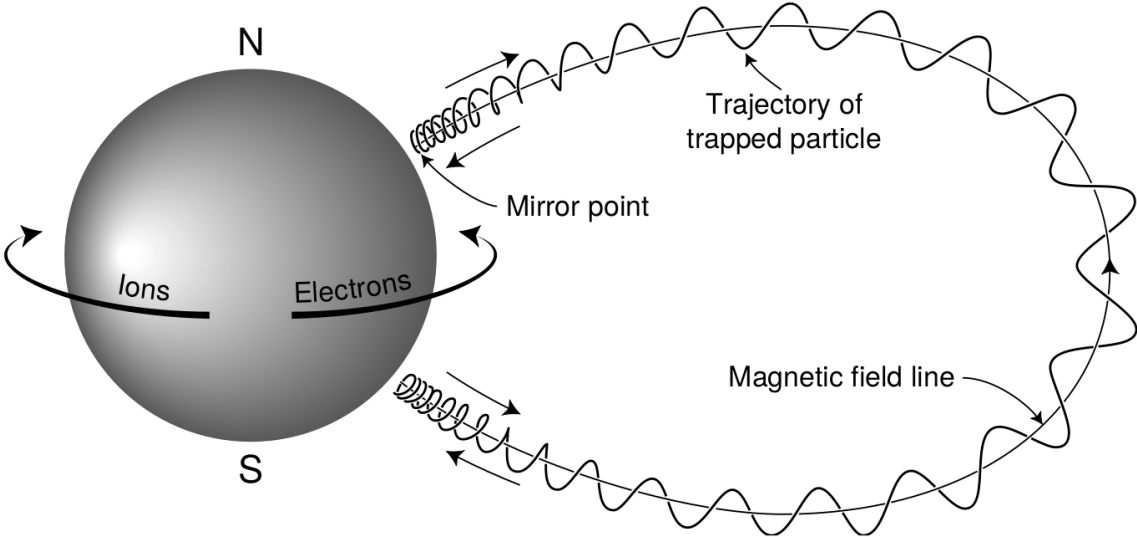


Figure 1.1: A diagram of the three motions that a charged particle experiences in Earth's dipole magnetic field. These motions are: gyration about the magnetic field line, bounce motion between the magnetic poles, and azimuthal drift around the Earth. Figure from (Baumjohann and Treumann, 1997).

experiences in an electric field \vec{E} and magnetic field \vec{B} and is given by

$$\frac{d\vec{p}}{dt} = q(\vec{E} + \vec{v} \times \vec{B}). \quad (1.1)$$

In the magnetosphere, the three periodic motions in decreasing frequency are gyration, bounce, and drift and are schematically shown in Fig. 1.1. Each of these periodic motions have a corresponding conserved quantity i.e. an adiabatic invariant.

The highest frequency periodic motion is on the order of a kHz in the magnetosphere and is gyration about a magnetic field of magnitude B . This motion is circular with a Larmor radius of

$$r = \frac{mv_{\perp}}{|q|B} \quad (1.2)$$

where m is the mass and v_{\perp} the particle velocity perpendicular to \vec{B} . This motion

has a corresponding gyrofrequency

$$\Omega = \frac{|q|B}{m} \quad (1.3)$$

in units of radians/second. The corresponding adiabatic invariant can be found by integrating the particle's canonical momentum around the particle's path

$$J_i = \oint (\vec{p} + q\vec{A}) \cdot d\vec{l} \quad (1.4)$$

where J_i is the i^{th} adiabatic invariant and \vec{A} is the magnetic vector potential. This integral is carried out by integrating the first term over the circumference of the gyro orbit and integrating the second term using Stokes theorem to calculate the magnetic flux enclosed by the gyro orbit. With suitable integration, $J_1 \sim v_{\perp}^2/B$ that is conserved as long as a driving force on the particle has a frequency much less than Ω .

The second highest frequency periodic motion is the bounce motion that is due to a parallel gradient in \vec{B} . This periodic motion naturally arises in the magnetosphere because the Earth's magnetic field is stronger near the poles, and artificially in the laboratory in magnetic bottle machines. First we need to define the concept of pitch angle α as the angle between the magnetic field and particle's velocity vectors. This is schematically shown in Fig. 1.2a. The pitch angle relates v with v_{\perp} , and v_{\parallel} (the component of the particles velocity parallel to \vec{B}). As shown in 1.2b and c, a larger α will tighten the particle's helix trajectory and vice versa.

Assuming that the particle's kinetic energy is concerned, the conservation of J_1 implies that given a particle's $v_{\perp}(0)$ and $B(0)$ at the magnetic equator, we can calculate its $v_{\perp}(s)$ along the particle's path with $B(s)$ from magnetic field models.

The perpendicular velocity is related via

$$\frac{v_{\perp}^2(0)}{B(0)} = \frac{v_{\perp}^2(s)}{B(s)} \quad (1.5)$$

which can be rewritten as

$$\frac{v^2 \sin^2 \alpha(0)}{B(0)} = \frac{v^2 - v_{\parallel}^2(s)}{B(s)} \quad (1.6)$$

and re-arranged to solve for $v_{\parallel}(s)$

$$v_{\parallel}(s) = v \sqrt{1 - \frac{B(s)}{B(0)} \sin^2 \alpha(0)} \quad (1.7)$$

which will tend towards 0 since $B(s) > B(0)$ in a dipole magnetic field.

The location where $v_{\parallel} = 0$ is called the mirror point where a particle stops and reverses direction. Since Earth's magnetic field is stronger towards the poles, the particle will execute periodic bounce motion between the two mirror points. The corresponding adiabatic invariant, J_2 is

$$J_2 = \oint p_{\parallel} ds \quad (1.8)$$

where ds describes the particle path between the mirror points in the northern and southern hemispheres (see Fig. 1.1). Substituting Eq. 1.7 into Eq. 1.8 and using the fact that at the mirror point the magnetic field strength is B_m and $\alpha(m) = 90^\circ$, J_2 can be written as

$$J_2 = 2p \int_{S \text{ mirror}}^{N \text{ mirror}} \sqrt{1 - \frac{B(s)}{B(m)}} ds \quad (1.9)$$

where $N \text{ mirror}$ and $S \text{ mirror}$ are the northern and southern mirror points, respectively. The bounce period can be estimated (e.g. Baumjohann and Treumann,

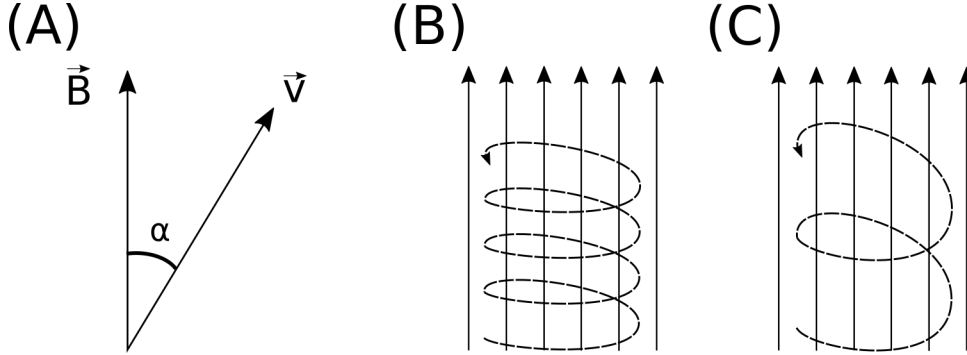


Figure 1.2: Charged particle motion in a uniform magnetic field \vec{B} . Panel (A) shows the geometry defining the pitch angle, α . Panel (B) and (C) show two helical electron trajectories assuming a large and small α (corresponding to a small and large parallel velocity $v_{||}$), respectively.

1997) to be

$$t_b \approx \frac{LR_e}{\sqrt{W/m}}(3.7 - 1.6 \sin \alpha_0) \quad (1.10)$$

where L is the L -shell which describes the distance from the Earth's center to where a particular magnetic field line crosses the magnetic equator, in units of Earth radii, R_e . W is the particle's kinetic energy, and α_0 is the equatorial pitch angle.

At this stage it is instructional to introduce the notion of the loss cone angle, α_L . α_L is defined such that if a charged particle has a $\alpha < \alpha_L$ it will mirror at or below ≈ 100 km altitude in the atmosphere. A particle at those altitudes will encounter Earth's atmosphere and has a significant probability of Coulomb scattering with atmospheric particles and be removed from the magnetosphere.

The slowest periodic motion experienced by charged particles in Earth's magnetic field is azimuthal drift around the Earth. This drift results from a combination of a radial gradient in \vec{B} and the curvature of the magnetic field. The radial gradient drift can be easily justified because Earth's magnetic field is stronger near the Earth where the particle's gyroradius radius of curvature will be smaller as it gyrates towards

the Earth, and larger when it gyrates outward. The overall effect is the particle gyro orbit does not close on itself and negatively charged particles drift East and negatively charged particles drift West. The drift due to the centrifugal force that a particle experiences as it bounces on curved field lines also increases the drift rate. The drift adiabatic invariant is found by integrating the J over the entire particle's orbit (drift shell) around the Earth. The first term is negligible, and the second term is the magnetic flux enclosed by the drift shell, Φ_m i.e. $J_3 \sim \Phi_m$.

Up until now the three drift motions conserve energy due to the absence of electric fields, \vec{E} . If \vec{E} is present, a particle's center of gyration (found by averaging over the gyro orbit) will drift in a direction perpendicular to both \vec{E} and \vec{B} . The drift velocity can be solved directly from Eq. 1.1 and is

$$\vec{v}_E = \frac{\vec{E} \times \vec{B}}{B^2}. \quad (1.11)$$

Lastly, detailed derivations of these motions can be found in (Baumjohann and Treumann, 1997; Schulz and Lanzerotti, 1974; Tsurutani and Lakhina, 1997).

Particle Populations and Their Interractions in the Magnetosphere

The single-particle motion described in the previous section was a prerequisite to understanding how these particles organize into macroscopic structures in the magnetosphere. The structure of the outer magnetosphere is shown in Fig. 1.4 and inner magnetosphere in Fig. 1.5. In this section we will discuss the macroscopic magnetosphere structures and how they couple.

The sun and its solar wind are ultimately the source of energy input into the magnetosphere. The solar wind at Earth is a plasma traveling at supersonic speeds with an embedded interplanetary magnetic field (IMF). When the solar wind

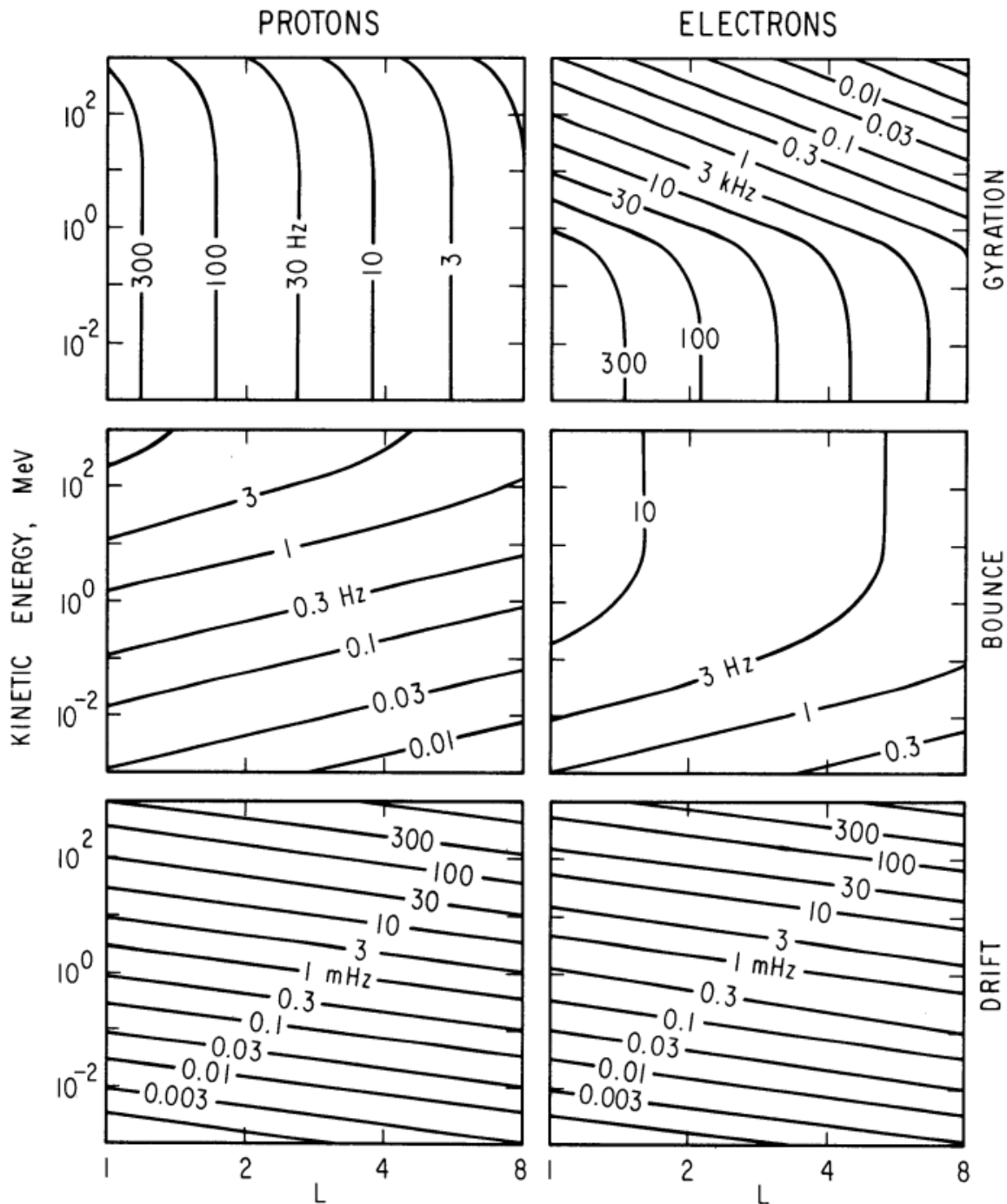


Figure 1.3: Contours of constant gyration, bounce, and drift frequencies for electrons and protons in a dipole field. Figure from Schulz and Lanzerotti (1974).

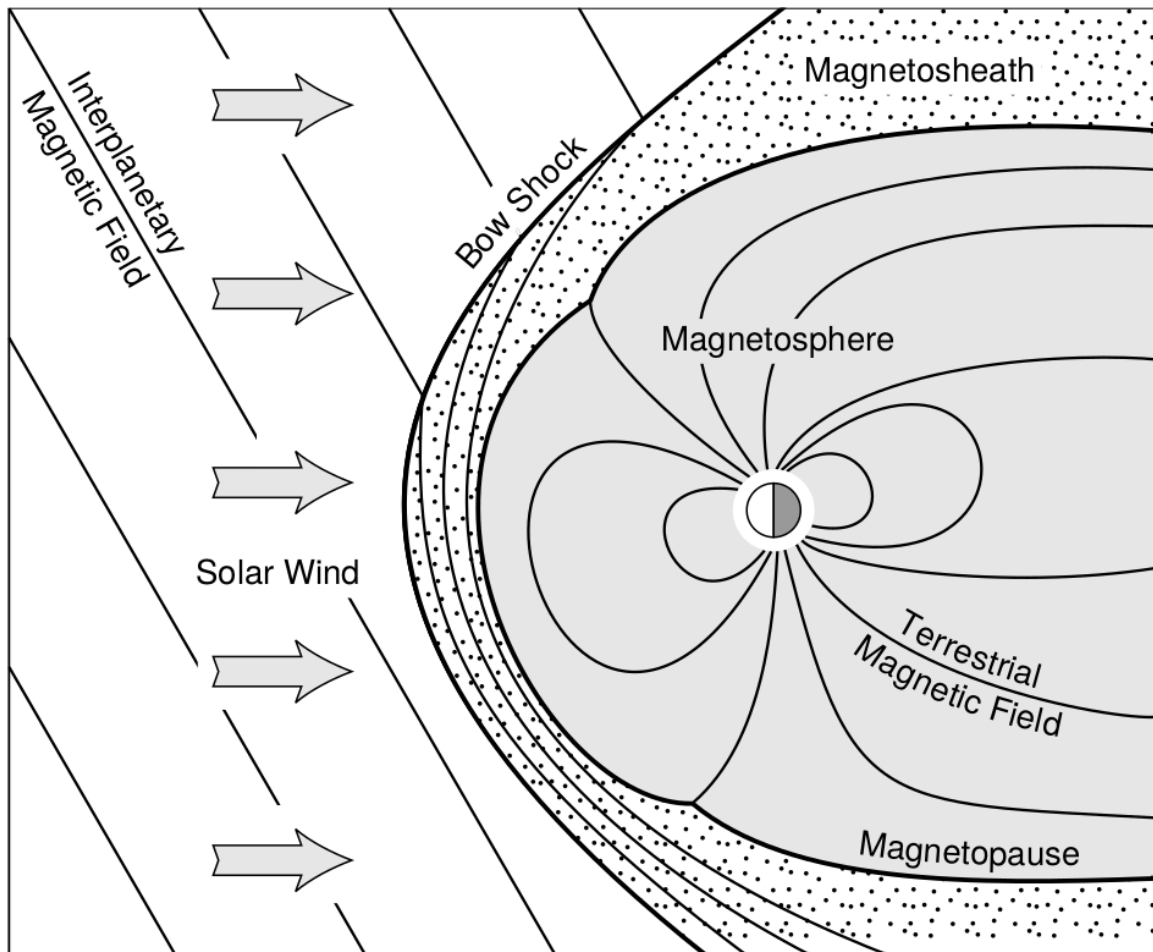


Figure 1.4: The large scale structures in the outer magnetosphere. The solar wind with its frozen-in interplanetary magnetic field is shown on the left and is traveling supersonically to the right. The solar wind envelops Earth's magnetic field to create the magnetosphere cavity. Since the solar wind is traveling supersonically, it creates a bow shock upstream. The shocked solar wind plasma in the magnetosheath flows around the magnetopause, a boundary between the solar wind and magnetosphere. Figure from Baumjohann and Treumann (1997).

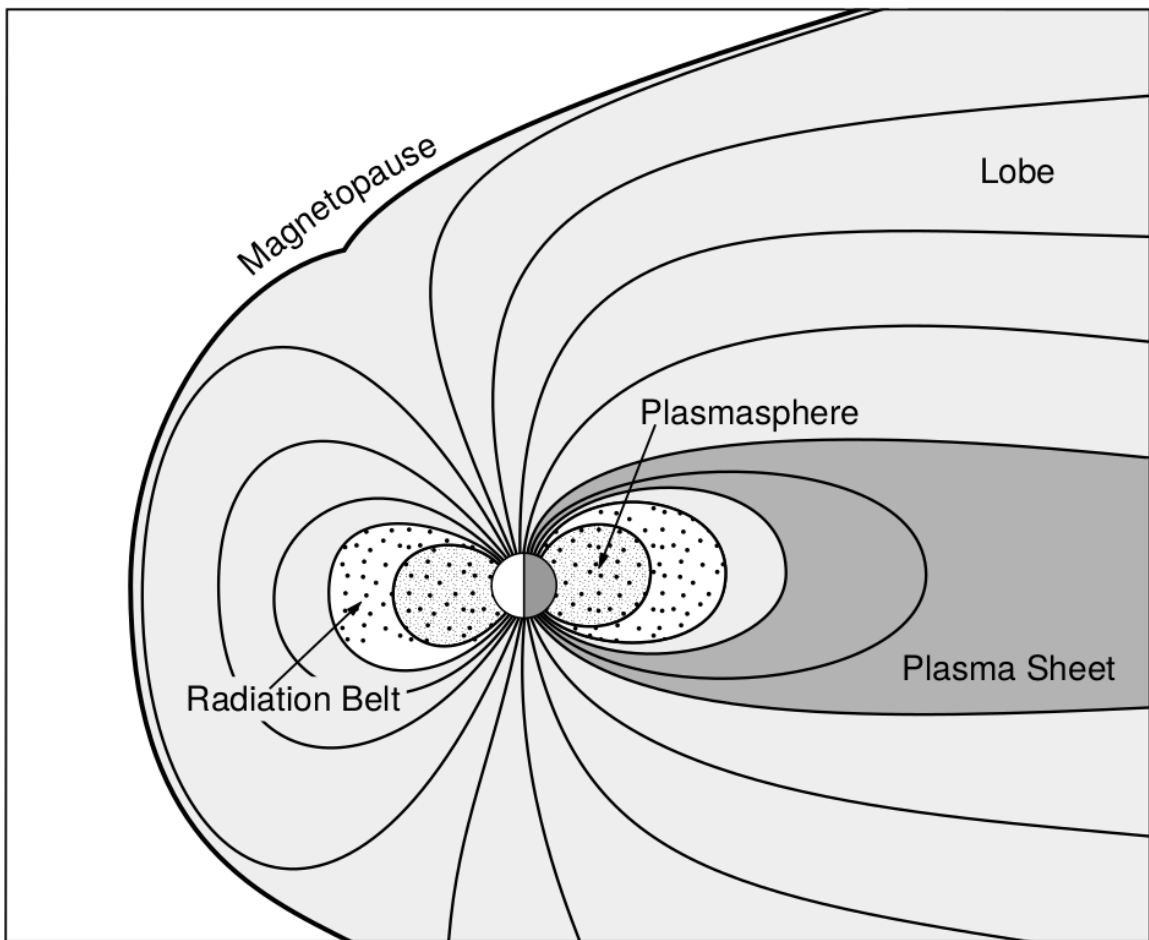


Figure 1.5: The large scale structures in the inner magnetosphere most relevant to this dissertation. The plasmasphere, and the radiation belts are shown and ring current is co-located there as well. Figure from Baumjohann and Treumann (1997).

encounters Earth's magnetic field the plasma can not easily penetrate into the magnetosphere, rather it drapes around the magnetosphere forming a cavity in the solar wind that is roughly shaped as shown in Figs. 1.4 and 1.5. Because the solar wind is supersonic at 1 AU, a bow shock exists upstream of the magnetosphere. The solar wind plasma, after it is shocked by the bow shock, then flows around the magnetosphere inside the magnetosheath. The surface where the solar wind ram and Earth's magnetic pressures balance is termed the magnetopause, which can be thought of as a boundary between the solar wind and Earth's plasma populations. This is a slightly naive description of the magnetopause, but is nonetheless an instructive conceptual picture. The shocked plasma then flows past the Earth where it carves out the magnetotail where the solar wind magnetic pressure balances Earth's magnetic field pressure in the lobes. The magnetotail extends on the order of 100 R_E downstream of Earth, and the tailward stretching of magnetic field lines creates the plasma sheet which exists in the region of low magnetic field strength near the magnetic equator. The plasma sheet flows from dusk to dawn (out of the page in Figs. 1.4 and 1.5) and this current is connected to a variety of other currents in the magnetosphere which is beyond the scope of this dissertation.

The idea of the magnetopause as a barrier between the solar wind and the magnetosphere is not entirely accurate due to the presence of reconnection. Reconnection was first conceived by Dungey (1961) who described the convection of Earth's magnetic field between the bow and tail regions of the magnetosphere. This process is known as the Dungey cycle and is most effective when the IMF is negative and pointing southward as is shown in 1 in Fig. 1.6. As the IMF contacts Earth's magnetic field it reconnects with it so that Earth's magnetic field is directly connected to the IMF. Then as the solar wind flows tailward the IMF drags Earth's magnetic field towards the magnetotail as shown in 2-6 in Fig. 1.6. As more and

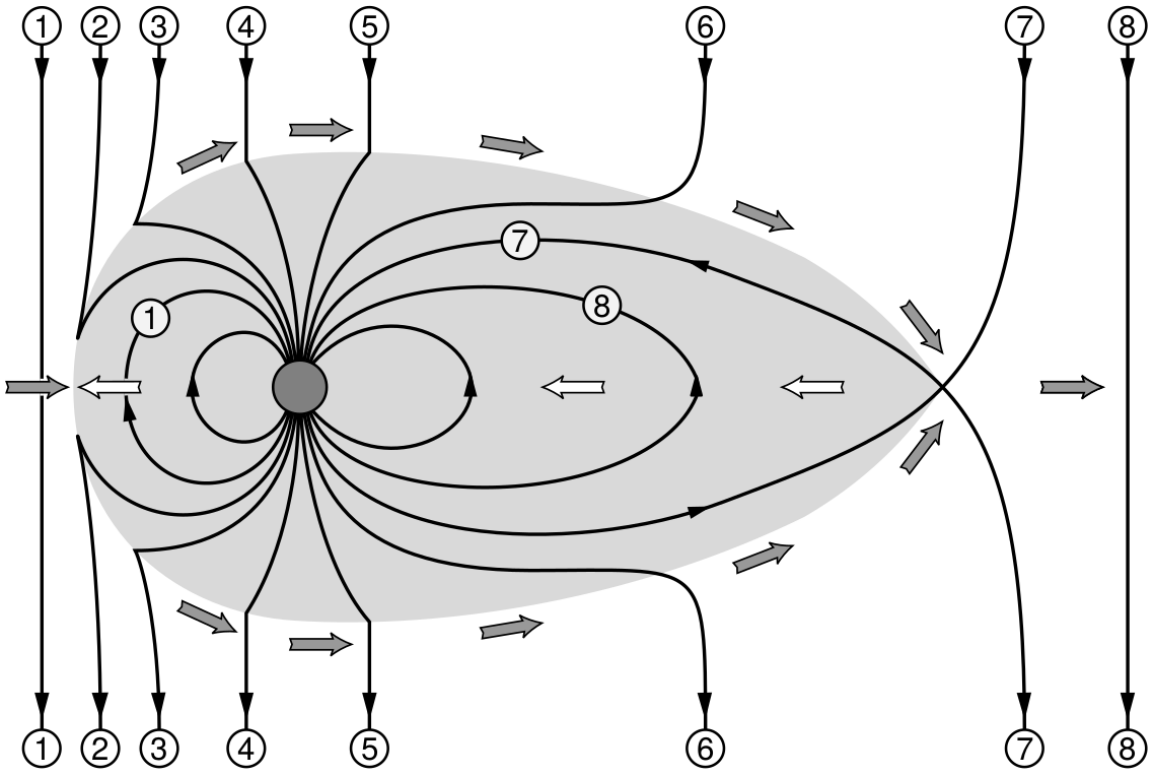


Figure 1.6: The series of steps involved in magnetic reconnection with a southward IMF. Figure from Baumjohann and Treumann (1997).

more magnetic field lines are draped in the magnetotail, magnetic pressure squeezes the plasma sheet until Earth's magnetic field reconnects as is shown in 7 in Fig. 1.6. Lastly as 8 in Fig. 1.6 shows, the newly merged magnetic field line and the plasma on it moves Earthward under the magnetic tension force to become more dipolar. This is called a dipolarization of the magnetic field, and the plasma frozen on these field lines can be observed as injections (e.g. Turner et al., 2015). These injections of plasma into the inner magnetosphere drives dynamics in the inner magnetosphere.

Inner Magnetosphere Populations

Before we describe the inner magnetosphere populations, we first need to describe the coordinate system used to organize the inner magnetosphere populations. The

first coordinate was defined in section 1 and is the L shell. L shell can be thought of as an analogue to a radius in a spherical geometry. The azimuthal coordinate is called the magnetic local time (MLT). For an observer above the north pole looking down, MLT (and its terminology) is defined to be 0 (midnight) in the anti-sunward direction, and increases in the counter-clockwise direction with 6 at dawn, 12 at noon (sunward direction), and 18 in dusk. The last coordinate used in this dissertation is the magnetic latitude, analogous to the latitude coordinate but referenced to the magnetic equator.

The low energy particle populations in the inner magnetosphere are organized by two electric fields: the co-rotation and the dawn-dusk electric fields. The co-rotation electric field arises from the rotation of Earth's magnetic field. Since particles are frozen on magnetic field lines and the plasma conductivity is effectively infinite, to a non-rotating observer this would appear as a radial electric field that drops off as $\sim L^2$. This electric field makes particles will orbit around the Earth due to the $\vec{E} \times \vec{B}$ drift. The other electric field, pointing from dawn to dusk is called the convection electric field and is formed by the Earthward movement of particles from the magnetotail that appears as an electric field to a stationary observer (with respect to Earth). The superposition of the co-rotation and convection electric fields results in a potential field shown in Fig. 1.7. The shaded area in Fig. 1.7 shows the orbits on which low energy electrons are trapped, and outside are the untrapped particles. The topology of the shaded region in Fig. 1.7 is controlled by the convection electric field which is dependent on the solar wind speed and the IMF. The low energy particles that are most effected by these electric fields make up the plasmasphere.

Plasmasphere The plasmasphere is a dense ($n_e \sim 10^3/\text{cm}^3$), cool plasma ($\sim \text{eV}$) that extends to $L \sim 4$ (extent is highly dependent on the solar wind and

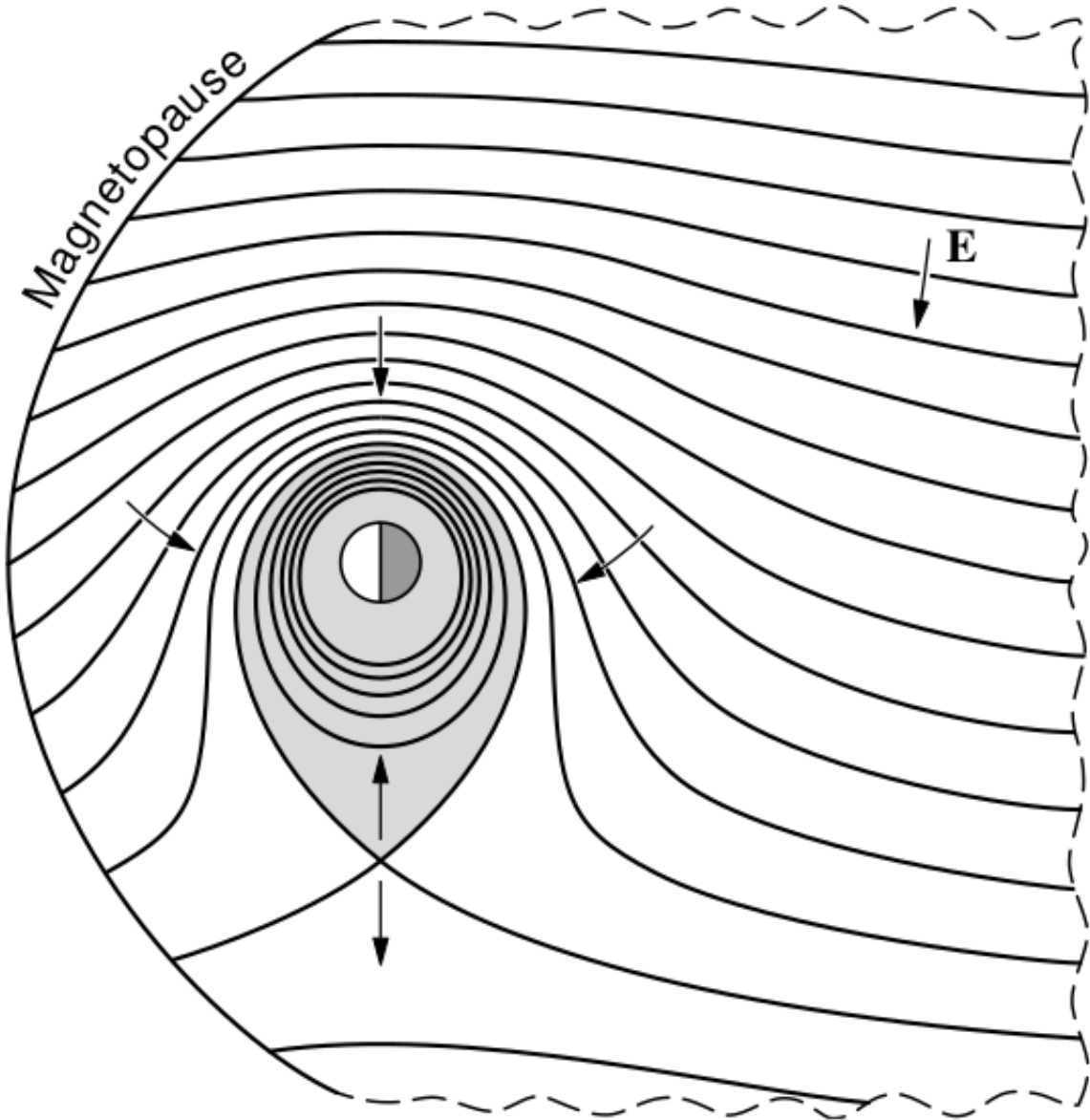


Figure 1.7: Equipotential lines and electric field (marked with arrows) due to the superposition of the co-rotation and convection electric fields. Electrons in the shaded region execute closed orbits. Outside of the shaded regions the electrons are not trapped and will escape. The region separating the two regimes is called the Alfvén layer. Figure from Baumjohann and Treumann (1997).

magnetospheric conditions) and is sourced from the ionosphere. The two dominant mechanisms that source the cold plasma from the ionosphere are ultraviolet ionization by sunlight and particle precipitation. The ultraviolet ionization is strongly dependent on the time of day (day vs night), latitude, and season and as we will see in the following sections, the ionization due to particle precipitation is dependent on particle energy, and mostly occurs at higher latitudes.

The outer boundary of the plasmasphere is the plasmapause which is typically defined as a steep radial gradient in plasma density from $\sim 10^3/\text{cm}^3$ to $\sim 1/\text{cm}^3$. As we will see throughout this dissertation, the location of the plasmapause is important to model (e.g. O'Brien and Moldwin, 2003) and understand since the plasma density strongly controls the efficiency of particle scattering (Horne et al., 2005).

Ring Current The next higher energy population is the ring current. This population consists of protons and electrons between tens and a few hundred keV that drift around the Earth. Since the direction of the drift due to the centrifugal and radial gradient forces is dependent on charge, protons drift west around the Earth and electrons drift East. This has the effect of creating a current around the Earth.

The ring current generates a magnetic field which decreases the magnetic field strength on Earth's surface and increases it outside of the ring current. The decrease of Earth's magnetic field strength is readily observed by a system of ground-based magnetometers and is merged into a Disturbance Storm Time (DST) index. An example of a DST index time series from the 2015 St. Patrick's Day storm is shown in Fig. 1.8. Figure 1.8 shows the effect that a coronal mass ejection (CME) has on the ring current. The ring current is sometimes first depleted (initial phase or sudden storm commencement; DST increases slightly). Then the ring current is rapidly built up (main phase; DST rapidly decreases). Lastly the ring current gradually returns

to its equilibrium state over a few day period (recovery phase; gradual increase in DST towards 0). The DST index along with other indices are readily used by the space physics community to loosely quantify the global state of the magnetosphere in modeling efforts.

Radiation Belts The highest energy particle populations are in the Van Allen radiation belts. These belts were discovered by Van Allen (1959) and Vernov and Chudakov (1960) during the Cold War and are a pair of toroidally shaped populations of trapped particles below $L \approx 8$ and are shown in Fig. 1.9. Their toroidal shape is a result of Earth's dipole magnetic field and the conservation of the three adiabatic invariants discussed in section 1.

The inner radiation belt is very stable on time periods of years, extends to $L \approx 2$, and mainly consists of protons with energies between MeV and GeV and electrons with energies up to ≈ 1 MeV (Claudepierre et al., 2019). The source of inner radiation belt protons is believed to be due to cosmic-ray albedo neutron decay (e.g. Li et al., 2017) Explain CRAND? and inward radial diffusion for electrons (e.g. O'Brien et al., 2016). The gap between the inner and outer radiation belt is called the slot, which is believed to be due to hiss waves inside the plasmasphere (described below) scattering electrons into the atmosphere (e.g. Breneman et al., 2015; Lyons and Thorne, 1973).

The outer radiation belt, on the other hand is much more dynamic and consists of mainly electrons of energies up to a few MeV. The outer belt's spatial extent is highly variable e.g. Fig. 1.10, and is typically observed at $4 < L < 8$. Since the outer radiation belt houses a dynamic population of energetic particles that pose a threat to humans and technology, decades of research has been undertaken to understand and predict the outer radiation belt particles and waves. The dynamics of the outer radiation belt can be split up into various competing acceleration and loss mechanisms

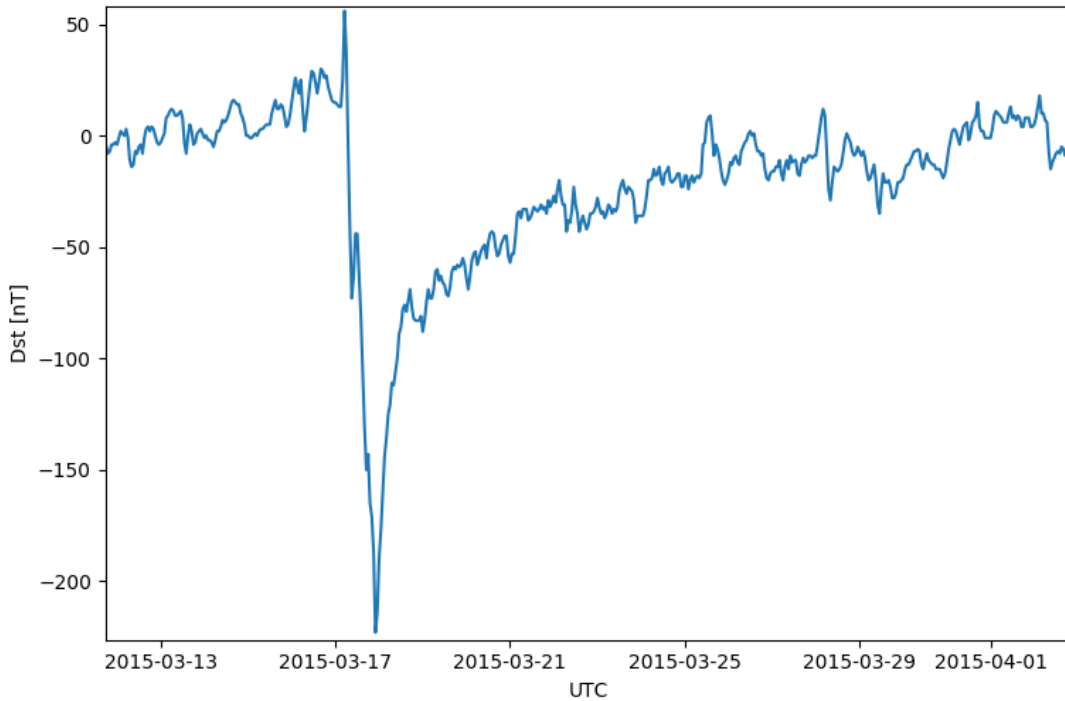


Figure 1.8: The DST index during the St. Patrick's Day 2015 storm. This storm was caused by a coronal mass ejection on March 15th, 2015. The storm phases are: initial phase, main phase, and recovery phase. The initial phase occurred when the Dst peaked at +50 nT on March 17th during which the ring current was eroded by the coronal mass ejection. The rapid decrease to ≈ -200 nT was during the main phase where many injections from the magnetotail pumped up the ring current which reduced Earth's magnetic field strength at the ground. Lastly, the recovery phase lasted from March 18th to approximately March 25th during which the ring current particles were lost and the magnetosphere returned to its equilibrium state.

The Earth's Electron Radiation Belts

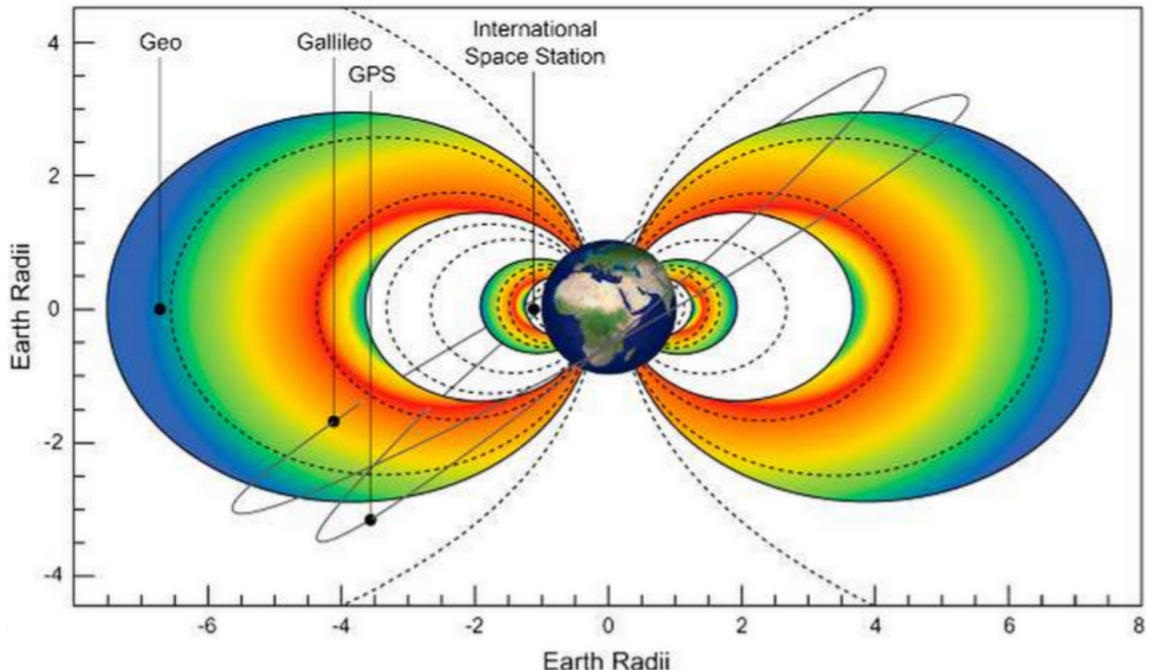


Figure 1.9: The two radiation belts with the locations of various satellites.
Figure from (Horne et al., 2013).

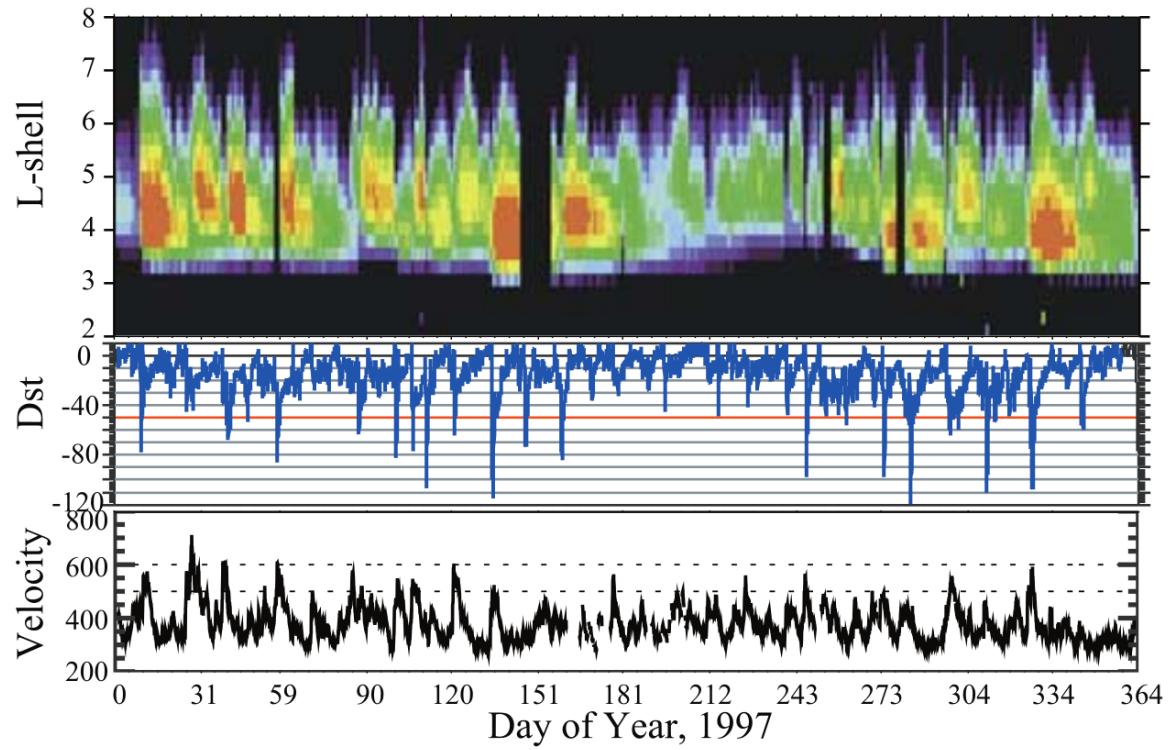


Figure 1.10: The dynamics of the outer radiation belt in 1997 from the POLAR satellite. Top panel shows the 1.2-2.4 MeV electron flux as a function of L and 1997 day of year. The middle panel shows the DST index, and bottom panel shows the solar wind velocity. Figure from (Reeves et al., 2003).

which will be described in the following sections.

Radiation Belt Particle Sources and Sinks

Adiabatic Heating

One of the particle heating mechanisms arises from the Earthward convection of particles. The conservation of J_1 implies that the initial and final v_{\perp} depends on the change in the magnetic field amplitude

$$\frac{v_{\perp i}^2}{B_i} = \frac{v_{\perp f}^2}{B_f} \quad (1.12)$$

and as a particle convects Earthward, $B_f > B_i$ so v_{\perp} must increase. The dipole magnetic field amplitude is

$$B(L, \theta) = \frac{31.2 \text{ } \mu\text{T}}{L^3} \sqrt{1 + 3 \cos^2 \theta} \quad (1.13)$$

which implies that

$$\frac{v_{\perp f}^2}{v_{\perp i}^2} = \left(\frac{L_i}{L_f} \right)^3 \quad (1.14)$$

Furthermore as the particle convects Earthward the mirror points on field lines start to converge. If J_2 is conserved, the decrease in the bounce path implies that $v_{||}$ must increase by

$$\frac{v_{|| f}^2}{v_{|| i}^2} = \left(\frac{L_i}{L_f} \right)^k \quad (1.15)$$

where k ranges from 2 for equatorial pitch angles, $\alpha_{eq} = 0^\circ$ to 2.5 for $\alpha_{eq} = 90^\circ$ (Baumjohann and Treumann, 1997). Since the rates of v_{\perp} adiabatic heating is greater

than the $v_{||}$ heating, an isotropic particle distribution will become anisotropic during its convection. These isotropic particles can then become unstable to wave growth and generate waves to reach equilibrium.

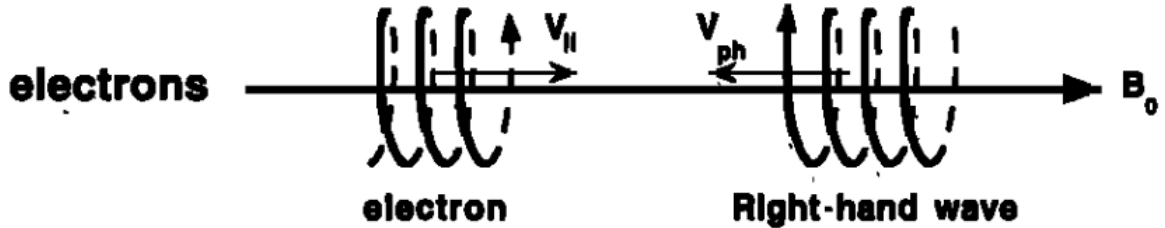
Wave Resonance Heating

A few of the electromagnetic wave modes responsible for particle acceleration (and deceleration) are whistler mode chorus (chorus) and electromagnetic ion cyclotron (EMIC) waves. These waves are created by the loss cone instability that is driven by an anisotropy of electrons for chorus waves, and protons for EMIC waves. The level of anisotropy can be quantified by the ratio of the perpendicular, T_{\perp} to parallel, $T_{||}$ particle temperatures such that the particle distribution is unstable when $T_{\perp}/T_{||} > 1$ which facilitates wave growth. Since the electrons are right-hand circularly polarized, the chorus waves also tend to be right hand circularly polarized (Tsurutani and Lakhina, 1997). The same argument applies to protons and EMIC waves as well.

These circularly polarized waves can resonate with electrons and/or protons since they are gyrating around the field line. One example of this is the cyclotron resonance pictorially shown in Fig. 1.21. An electron's $v_{||}$ and the parallel wave vector $k_{||}$ are in opposite directions such that the wave frequency ω is Doppler shifted to an integer multiple of the Ω_e at which point the electron feels a static electric field and is accelerated (decelerated). This happens when a resonance condition is satisfied which we will now derive in the simplest case.

Assume a uniform magnetic field $\vec{B} = B_0 \hat{z}$ with a parallel propagating ($k = k\hat{z}$), right-hand circularly polarized wave

$$\vec{E} = E_0(\cos \omega t - kz\hat{x} + \sin \omega t - kz\hat{y}) \quad (1.16)$$



$$\omega + \mathbf{k}_{\parallel} \mathbf{V}_{\parallel} = \Omega^-$$

Figure 1.11: The trajectories of an electron and a right-hand circularly polarized wave when a cyclotron resonance can occur. The electron's v_{\parallel} and the wave's k_{\parallel} are in opposite directions such that the wave's frequency is Doppler shifted to an integer multiple of the electron cyclotron frequency. Figure from (Tsurutani and Lakhina, 1997).

which can be used to take the dot product to find its angular component

$$E_{\theta} = \vec{E} \times \hat{\theta} = E_0 \cos \omega t - kz + \theta \quad (1.17)$$

where θ is the particle phase. Now assume the electron is traveling in the $-\hat{z}$ direction with a velocity $\vec{v} = -v_0 \hat{z}$ and its time dependent position along \hat{z} is

$$z(t) = v_0 t \quad (1.18)$$

and gyrophase is

$$\theta(t) = -\Omega t + \theta(0) \quad (1.19)$$

where the first negative sign comes from the electron's negative charge. Now we put this all together and express the electric field and the force that the electron will

experience

$$m \frac{dv_\theta}{dt} = qE_\theta = qE_0 \sin((\omega + kv_0 - \Omega)t - \theta(0)). \quad (1.20)$$

This is a relatively complex expression, but when the time dependent component,

$$\omega + kv_0 - \Omega = 0, \quad (1.21)$$

the electron will be in a static electric field which will accelerate or decelerate the electron depending on θ_0 , the phase between the wave and the electron. [Show Bortnik 2008 plot?](#) The expression in Eq. 1.21 is commonly referred to as the resonance condition. A few wave modes that a particle experiences along its drift orbit and are relevant to particle scattering studied here are shown in Fig. 1.12.

Particle Losses

There are various transport or scatter mechanisms that result in the loss of radiation belt particles into the atmosphere or the solar wind. One of the loss mechanisms of particles into the solar wind is magnetopause shadowing (Ukhorskiy et al., 2006). Recall that when the ring current is strengthened, the magnetic field is reduced on Earth's surface and increased outside of the ring current. If the time scale of the ring current strengthening is slower than a particle drift, the third adiabatic invariant is conserved. In order to conserve the third adiabatic invariant while the magnetic field strength is increasing outside of the ring current, the particle's orbit gradually moves outward. If the particle drift shell crosses the magnetopause the particle will then be lost to the solar wind.

[Move to acceleration?](#) Another particle loss (and acceleration) mechanism is driven by ultra low frequency (ULF) waves and is called radial diffusion. Radial

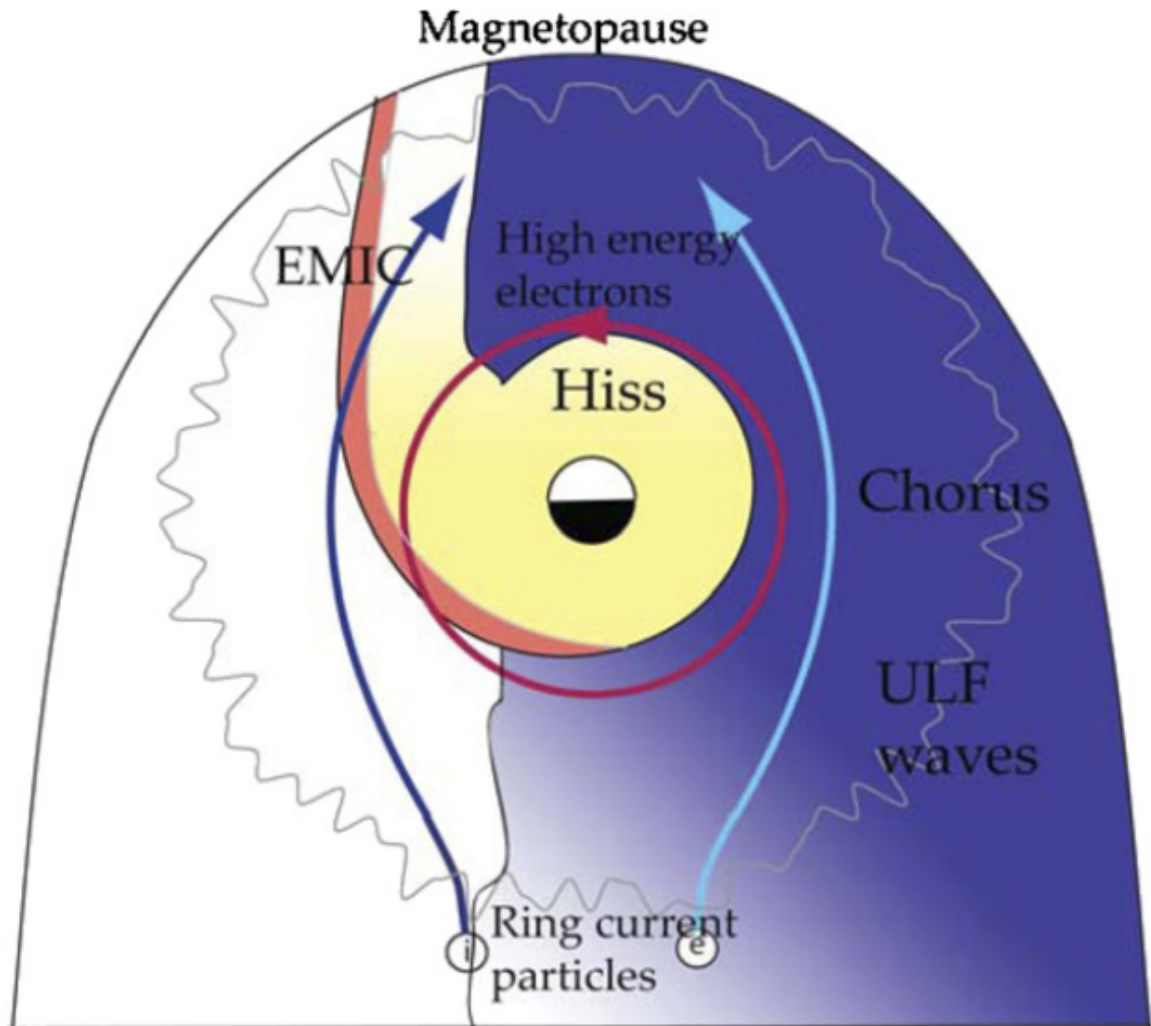


Figure 1.12: Various wave modes in the magnetosphere. Ultra low frequency waves occur through the magnetosphere. Chorus waves are typically observed in the 0-12 midnight-dawn region. EMIC waves are typically observed in the dusk MLT sector. Hiss waves are observed inside the plasmasphere. Figure from Millan and Thorne (2007).

diffusion is the transport of particles from high to low phase space density, f . If the transport is radially inward, particles will appear to be accelerated. On the other hand, radially outward radial diffusion can transport particles through the magnetopause where they will be lost. Reeves et al. (2013) investigated the driver of particle acceleration during the October 2012 storm and observationally found that inward radial diffusion was not dominant, rather local acceleration via pitch angle diffusion which will be described below appeared to be the dominant acceleration mechanism.

The loss mechanism central to this dissertation is pitch angle and energy scattering of electrons by waves such as plasmaspheric hiss (e.g. Breneman et al., 2015), EMIC waves (e.g. Capannolo et al., 2019), and chorus waves (e.g. Breneman et al., 2017). These wave-particle interactions occur when the resonance condition in Eq. 1.21 is satisfied. When it is satisfied the particle's energy and α is modified by the wave. If the wave changes α towards 0 such that $\alpha < \alpha_{LC}$, the particle's mirror point lowers below ≈ 100 km altitude and can be lost due collisions with air. Some of these electrons can be impulsively scattered into the loss cone where they are observed as a sub second duration enhancements termed microbursts.

Microbursts

Anderson and Milton (1964) first reported microbursts from high altitude balloon observations of bremsstrahlung X-rays emitted by microburst electrons impacting the atmosphere. Over the decades since then, microbursts have been observed on many other balloon missions (e.g. Anderson et al., 2017; Parks, 1967; Woodger et al., 2015). In addition to the X-ray signature, microbursts electrons have been directly observed in LEO with LEO spacecraft including the Solar Anomalous and Magnetospheric Particle Explorer (SAMPEX), Focused Investigation

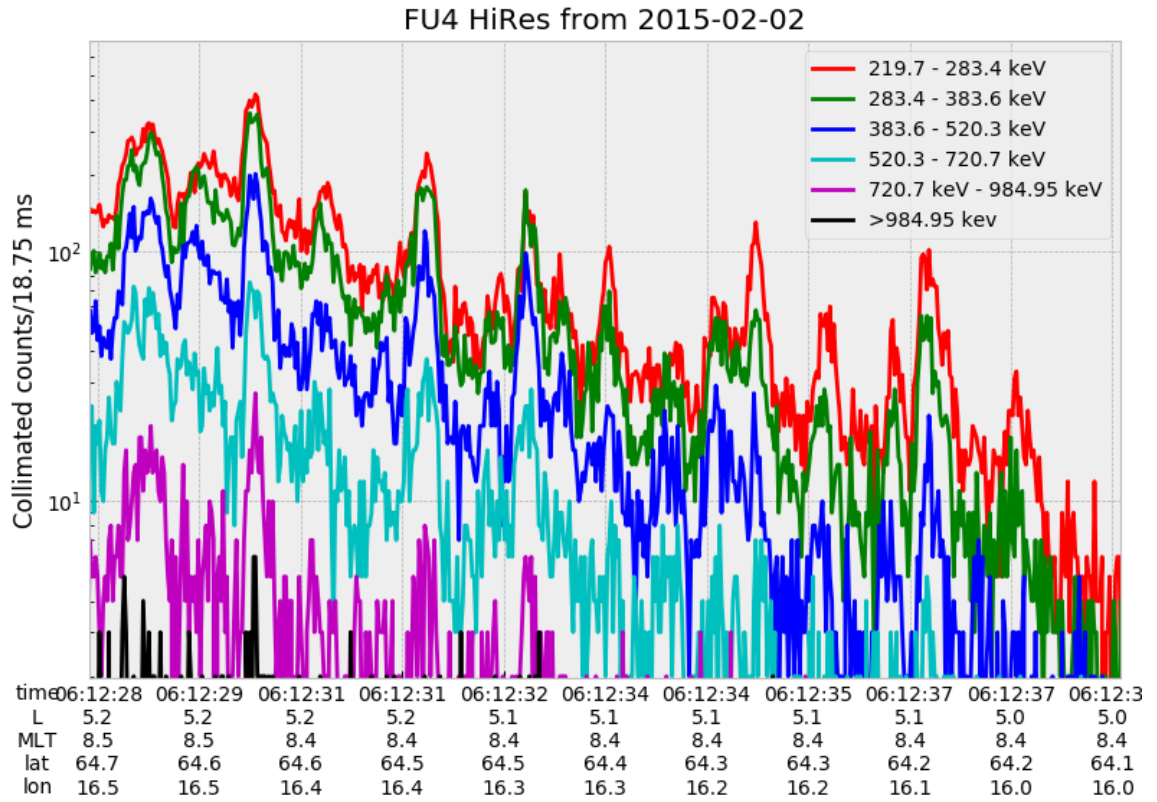


Figure 1.13: An example train of microbursts observed by FIREBIRD-II unit 4 on February 2nd, 2015. The colored curves show the differential energy channel count rates in six channels from ≈ 200 keV to greater than 1 MeV. The x-axis labels show auxiliary information such as time of observation and the spacecraft position in L, MLT, latitude and longitude coordinates.

of Relativistic Electron Bursts: Intensity, Range, and Dynamics II (FIREBIRD-II), Science Technologies Satellite (STSAT-I) (e.g. Blake et al., 1996; Blum et al., 2015; Breneman et al., 2017; Crew et al., 2016; Lee et al., 2012, 2005; Lorentzen et al., 2001a,b; Nakamura et al., 1995, 2000; O'Brien et al., 2004, 2003). An example microburst time series is shown in Fig. 1.13.

Microbursts are observed on magnetic field footprints that are connected to the outer radiation belt, and are predominately observed in the 0-12 MLT sector

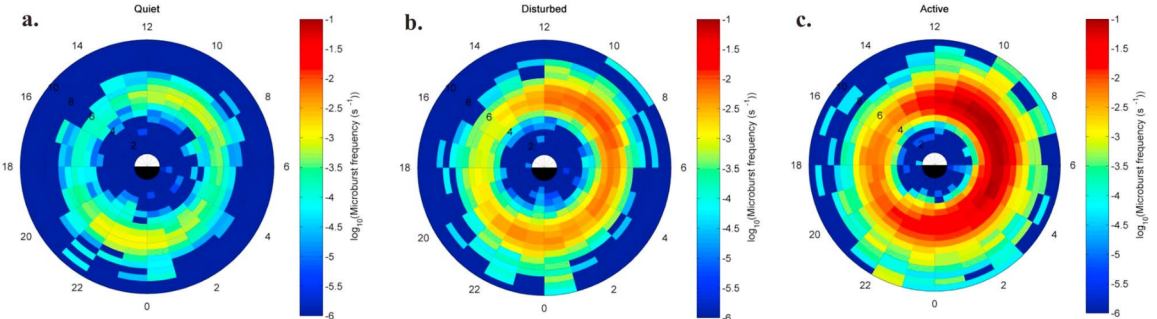


Figure 1.14: Relativistic ($> 1\text{MeV}$) distribution of microburst occurrence rates as a function of L and MLT. The three panels explore the microburst occurrence rate dependence on geomagnetic activity parameterized by the auroral electrojet index for (a) $\text{AE} < 100 \text{nT}$, (b) $100 < \text{AE} < 300 \text{nT}$ and (c) $\text{AE} > 300 \text{nT}$. Figure from Douma et al. (2017).

with an elevated occurrence frequency during disturbed times as shown in Fig. 1.14. Microbursts have been observed over a wide energy range from a few tens of keV (Datta et al., 1997) to greater than 1 MeV (e.g. Blake et al., 1996; Greeley et al., 2019). The microburst electron flux (J) vs energy spectra is typically well fit to a decaying exponential (e.g. (Lee et al., 2005; Parks, 1967))

$$J(E) = J_0 e^{-E/E_0} \quad (1.22)$$

where J_0 is the flux at 0 keV (unphysical free parameter) and E_0 quantifies the efficiency of the scattering mechanism in energy. A small E_0 suggests that mostly high energy particles are scattered and a high E_0 suggests that the scattering mechanism scatters low and high energy electrons. In reality, a high E_0 may be a signature of a high energy electron scattering mechanism, but is hidden by the convolution of the source particles available to be scattered (typically with a falling energy spectrum) and the energy-dependent scattering efficiency.

The short microburst duration observed by a single LEO satellite creates an

ambiguity in interpreting what is exactly a microbursts. Is a microburst very small and spatially stationary so that the LEO spacecraft flies through it in less than a second, or are microbursts large, but short duration such that the microburst comes and goes in a fraction of a second? A high altitude balloon provides essentially a stationary view of the radiation belt footprints and a temporal microburst can be unambiguously identified, but a spatial structure is very difficult to identify.

Multi-spacecraft missions are better equipped to determine if a microburst is spatial or temporal. As will be shown in this dissertation, if a microburst is observed simultaneously by two spacecraft then it is temporally transient with a size greater than the spacecraft separation. On the other hand, if two spacecraft observe a microburst-like feature in the same location and at different times, then it is spatial and called a curtain (Blake and O'Brien, 2016).

the microburst size and if it is spatial or temporal, and a balloon can easily observe the temporal microbursts but have limited spatial information. Both observation methods have a unique set of strengths and weaknesses, and this dissertation takes the multi-spacecraft approach to analyze the size of microbursts.

Scope of Reserach

This dissertation furthers our understanding of the microburst scattering mechanism and is organized into the following chapters. Chapter X will describe the spacecraft missions used to study microburst precipitation and wave-particle scattering. Then Ch. Y will describe a microburst scattering event observed by NASA's Van Allen Probes and the quasi-linear diffusion model that was developed. Next, Ch. Z will describe a bouncing packet microburst observation made by MSU's FIREBIRD-II mission where the microburst's lower bound longitudinal and latitudinal scale sizes were estimated. Chapter ZZ then expands the case study result

from Ch. **Z** to a statistical study of microburst sizes and the microburst size models developed to interpret the data. Lastly, **ZZZ** will summarize the dissertation work and make concluding remarks about research to be done.

Mention a theme for the three papers.

Bibliography

- Anderson, B., Shekhar, S., Millan, R., Crew, A., Spence, H., Klumpar, D., Blake, J., O'Brien, T., and Turner, D. (2017). Spatial scale and duration of one microburst region on 13 August 2015. *Journal of Geophysical Research: Space Physics*.
- Anderson, K. A. and Milton, D. W. (1964). Balloon observations of X rays in the auroral zone: 3. High time resolution studies. *Journal of Geophysical Research*, 69(21):4457–4479.
- Baumjohann, W. and Treumann, R. A. (1997). *Basic space plasma physics*. World Scientific.
- Blake, J.,Looper, M., Baker, D., Nakamura, R., Klecker, B., and Hovestadt, D. (1996). New high temporal and spatial resolution measurements by sampex of the precipitation of relativistic electrons. *Advances in Space Research*, 18(8):171 – 186.
- Blake, J. B. and O'Brien, T. P. (2016). Observations of small-scale latitudinal structure in energetic electron precipitation. *Journal of Geophysical Research: Space Physics*, 121(4):3031–3035. 2015JA021815.
- Blum, L., Li, X., and Denton, M. (2015). Rapid MeV electron precipitation as observed by SAMPEX/HILT during high-speed stream-driven storms. *Journal of Geophysical Research: Space Physics*, 120(5):3783–3794. 2014JA020633.
- Breneman, A., Crew, A., Sample, J., Klumpar, D., Johnson, A., Agapitov, O., Shumko, M., Turner, D., Santolik, O., Wygant, J., et al. (2017). Observations directly linking relativistic electron microbursts to whistler mode chorus: Van allen probes and FIREBIRD II. *Geophysical Research Letters*.
- Breneman, A. W., Halford, A., Millan, R., McCarthy, M., Fennell, J., Sample, J., Woodger, L., Hospodarsky, G., Wygant, J. R., Cattell, C. A., et al. (2015). Global-scale coherence modulation of radiation-belt electron loss from plasmaspheric hiss. *Nature*, 523(7559):193.
- Capannolo, L., Li, W., Ma, Q., Shen, X.-C., Zhang, X.-J., Redmon, R., Rodriguez, J., Engebretson, M., Kletzing, C., Kurth, W., et al. (2019). Energetic electron precipitation: multi-event analysis of its spatial extent during emic wave activity. *Journal of Geophysical Research: Space Physics*.
- Claudepierre, S., O'Brien, T., Looper, M., Blake, J., Fennell, J., Roeder, J., Clemmons, J., Mazur, J., Turner, D., Reeves, G., et al. (2019). A revised look at relativistic electrons in the earth's inner radiation zone and slot region. *Journal of Geophysical Research: Space Physics*, 124(2):934–951.

- Crew, A. B., Spence, H. E., Blake, J. B., Klumpar, D. M., Larsen, B. A., O'Brien, T. P., Driscoll, S., Handley, M., Legere, J., Longworth, S., Mashburn, K., Mosleh, E., Ryhajlo, N., Smith, S., Springer, L., and Widholm, M. (2016). First multipoint in situ observations of electron microbursts: Initial results from the NSF FIREBIRD II mission. *Journal of Geophysical Research: Space Physics*, 121(6):5272–5283. 2016JA022485.
- Datta, S., Skoug, R., McCarthy, M., and Parks, G. (1997). Modeling of microburst electron precipitation using pitch angle diffusion theory. *Journal of Geophysical Research: Space Physics*, 102(A8):17325–17333.
- Douma, E., Rodger, C. J., Blum, L. W., and Clilverd, M. A. (2017). Occurrence characteristics of relativistic electron microbursts from SAMPEX observations. *Journal of Geophysical Research: Space Physics*, 122(8):8096–8107. 2017JA024067.
- Dungey, J. W. (1961). Interplanetary magnetic field and the auroral zones. *Phys. Rev. Lett.*, 6:47–48.
- Greeley, A., Kanekal, S., Baker, D., Klecker, B., and Schiller, Q. (2019). Quantifying the contribution of microbursts to global electron loss in the radiation belts. *Journal of Geophysical Research: Space Physics*.
- Horne, R., Glauert, S., Meredith, N., Boscher, D., Maget, V., Heynderickx, D., and Pitchford, D. (2013). Space weather impacts on satellites and forecasting the earth's electron radiation belts with spacecast. *Space Weather*, 11(4):169–186.
- Horne, R. B., Thorne, R. M., Shprits, Y. Y., Meredith, N. P., Glauert, S. A., Smith, A. J., Kanekal, S. G., Baker, D. N., Engebretson, M. J., Posch, J. L., et al. (2005). Wave acceleration of electrons in the van allen radiation belts. *Nature*, 437(7056):227.
- Lee, J. J., Parks, G. K., Lee, E., Tsurutani, B. T., Hwang, J., Cho, K. S., Kim, K.-H., Park, Y. D., Min, K. W., and McCarthy, M. P. (2012). Anisotropic pitch angle distribution of 100 keV microburst electrons in the loss cone: measurements from STSAT-1. *Annales Geophysicae*, 30(11):1567–1573.
- Lee, J.-J., Parks, G. K., Min, K. W., Kim, H. J., Park, J., Hwang, J., McCarthy, M. P., Lee, E., Ryu, K. S., Lim, J. T., Sim, E. S., Lee, H. W., Kang, K. I., and Park, H. Y. (2005). Energy spectra of 170–360 keV electron microbursts measured by the korean STSAT-1. *Geophysical Research Letters*, 32(13). L13106.
- Li, X., Selesnick, R., Schiller, Q., Zhang, K., Zhao, H., Baker, D. N., and Temerin, M. A. (2017). Measurement of electrons from albedo neutron decay and neutron density in near-earth space. *Nature*, 552(7685):382.

- Lorentzen, K. R., Blake, J. B., Inan, U. S., and Bortnik, J. (2001a). Observations of relativistic electron microbursts in association with VLF chorus. *Journal of Geophysical Research: Space Physics*, 106(A4):6017–6027.
- Lorentzen, K. R.,Looper, M. D., and Blake, J. B. (2001b). Relativistic electron microbursts during the GEM storms. *Geophysical Research Letters*, 28(13):2573–2576.
- Lyons, L. R. and Thorne, R. M. (1973). Equilibrium structure of radiation belt electrons. *Journal of Geophysical Research*, 78(13):2142–2149.
- Millan, R. and Thorne, R. (2007). Review of radiation belt relativistic electron losses. *Journal of Atmospheric and Solar-Terrestrial Physics*, 69(3):362 – 377.
- Nakamura, R., Baker, D. N., Blake, J. B., Kanekal, S., Klecker, B., and Hovestadt, D. (1995). Relativistic electron precipitation enhancements near the outer edge of the radiation belt. *Geophysical Research Letters*, 22(9):1129–1132.
- Nakamura, R., Isowa, M., Kamide, Y., Baker, D., Blake, J., and Looper, M. (2000). Observations of relativistic electron microbursts in association with VLF chorus. *J. Geophys. Res.*, 105:15875–15885.
- O'Brien, T., Claudepierre, S., Guild, T., Fennell, J., Turner, D., Blake, J., Clemmons, J., and Roeder, J. (2016). Inner zone and slot electron radial diffusion revisited. *Geophysical Research Letters*, 43(14):7301–7310.
- O'Brien, T. and Moldwin, M. (2003). Empirical plasmapause models from magnetic indices. *Geophysical Research Letters*, 30(4).
- O'Brien, T. P., Looper, M. D., and Blake, J. B. (2004). Quantification of relativistic electron microburst losses during the GEM storms. *Geophysical Research Letters*, 31(4). L04802.
- O'Brien, T. P., Lorentzen, K. R., Mann, I. R., Meredith, N. P., Blake, J. B., Fennell, J. F., Looper, M. D., Milling, D. K., and Anderson, R. R. (2003). Energization of relativistic electrons in the presence of ULF power and MeV microbursts: Evidence for dual ULF and VLF acceleration. *Journal of Geophysical Research: Space Physics*, 108(A8).
- Parks, G. K. (1967). Spatial characteristics of auroral-zone X-ray microbursts. *Journal of Geophysical Research*, 72(1):215–226.
- Reeves, G., Spence, H. E., Henderson, M., Morley, S., Friedel, R., Funsten, H., Baker, D., Kanekal, S., Blake, J., Fennell, J., et al. (2013). Electron acceleration in the heart of the van allen radiation belts. *Science*, 341(6149):991–994.

- Reeves, G. D., McAdams, K. L., Friedel, R. H. W., and O'Brien, T. P. (2003). Acceleration and loss of relativistic electrons during geomagnetic storms. *Geophysical Research Letters*, 30(10):n/a–n/a. 1529.
- Schulz, M. and Lanzerotti, L. J. (1974). *Particle Diffusion in the Radiation Belts*. Springer.
- Tsurutani, B. T. and Lakhina, G. S. (1997). Some basic concepts of wave-particle interactions in collisionless plasmas. *Reviews of Geophysics*, 35(4):491–501.
- Turner, D., Claudepierre, S., Fennell, J., O'Brien, T., Blake, J., Lemon, C., Gkioulidou, M., Takahashi, K., Reeves, G., Thaller, S., et al. (2015). Energetic electron injections deep into the inner magnetosphere associated with substorm activity. *Geophysical Research Letters*, 42(7):2079–2087.
- Ukhorskiy, A. Y., Anderson, B. J., Brandt, P. C., and Tsyganenko, N. A. (2006). Storm time evolution of the outer radiation belt: Transport and losses. *Journal of Geophysical Research: Space Physics*, 111(A11):n/a–n/a. A11S03.
- Van Allen, J. A. (1959). The geomagnetically trapped corpuscular radiation. *Journal of Geophysical Research*, 64(11):1683–1689.
- Vernov, S. and Chudakov, A. (1960). Investigation of radiation in outer space. In *International Cosmic Ray Conference*, volume 3, page 19.
- Woodger, L., Halford, A., Millan, R., McCarthy, M., Smith, D., Bowers, G., Sample, J., Anderson, B., and Liang, X. (2015). A summary of the BARREL campaigns: Technique for studying electron precipitation. *Journal of Geophysical Research: Space Physics*, 120(6):4922–4935.